



Central shutdown and surrounding activation of aftershocks from megathrust earthquake stress transfer

Shinji Toda ^{□1⊠} and Ross S. Stein ^{□2⊠}

Megathrust earthquakes release and transfer stress that has accumulated over hundreds of years, leading to large aftershocks that can be highly destructive. Understanding the spatiotemporal pattern of megathrust aftershocks is key to mitigating the seismic hazard. However, conflicting observations show aftershocks concentrated either along the rupture surface itself, along its periphery or well beyond it, and they can persist for a few years to decades. Here we present aftershock data following the four largest megathrust earthquakes since 1960, focusing on the change in seismicity rate following the best-recorded 2011 Tohoku earthquake, which shows an initially high aftershock rate on the rupture surface that quickly shuts down, while a zone up to ten times larger forms a ring of enhanced seismicity around it. We find that the aftershock pattern of Tohoku and the three other megathrusts can be explained by rate and state Coulomb stress transfer. We suggest that the shutdown in seismicity in the rupture zone may persist for centuries, leaving seismicity gaps that can be used to identify prehistoric megathrust events. In contrast, the seismicity of the surrounding area decays over 4-6 decades, increasing the seismic hazard after a megathrust earthquake.

eismic hazard assessments, which guide mitigation strategies for the public and financial risk transfer for industry, are generally based on long-term or slowly changing earthquake rates. However, megathrusts and other large mainshocks cause the hazard to depart abruptly from its average behaviour, including the occurrence of damaging aftershocks and progressive mainshocks^{1,2}. Observations that subduction aftershocks are concentrated in or along the periphery of the rupture surface³⁻⁶ contrast with observations that aftershocks surround or extend well beyond the rupture⁷⁻¹¹. The duration of megathrust aftershock sequences is also debated: from several years^{11,12} to a decade or more^{11,13}.

To improve seismic hazard assessments, seismologists seek to distinguish aftershocks from background earthquakes, and to forecast aftershock distribution and temporal decay, by using approaches such as the Epidemic Type Aftershock Sequence¹⁴ and its predecessors. These models assume that mainshocks produce seismicity rate increases, with the greatest increases close to or on the rupture surface. The alternative approach views aftershocks as promoted by Coulomb stress transfer, locating where the mainshock rupture increased the shear stress on surrounding faults, or unclamped them¹⁵. However, as seismic networks have improved, it has become evident that mainshocks can also reduce the seismicity rate on faults on which the Coulomb stress imparted by the mainshock has decreased^{16,17}. Here, we show that the disparate observations of megathrust aftershocks can be explained by a single Coulomb hypothesis, which can be used both to forecast aftershocks and to hunt for prehistoric megathrusts.

Observed spatiotemporal pattern of megathrust aftershocks

Within five years of the $M \ge 9$ shocks that have struck since 1960, aftershocks on the high-slip portions of the rupture surface had largely shut down (Fig. 1). This includes the 2011 M9.0 Tohoku,

1964 M9.2 Prince William Sound, 2004 M9.2 Sumatra and 1960 M9.5 Valdivia earthquakes. For Valdivia the aftershocks appear to have shut down within months, whereas for the others they shut down within 1–3 yr. For all these events, a surrounding annulus of seismicity activated immediately, and continues to be active today, up to 60 yr later.

Due to Japan's high-quality seismic network, the 2011 M9.0 Tohoku earthquake furnishes the best event to probe more deeply. In Fig. 2a, we compare the seismicity during the period 5–10 yr after the mainshock with the background period, chosen to be as long as possible above the magnitude of completeness¹⁸, in this case 13 yr preceding the mainshock. The seismicity rate in the core, which coincides with the area of peak coseismic slip¹⁹, has dropped by a factor of three to five below the background rate. The Omori aftershock decay slope p is also steeper and the earthquake magnitudes smaller in the rupture zone than in the surrounding region (Extended Data Fig. 1). A smaller disc of seismicity rate drop is seen at the site of the M7.9 aftershock, which struck 30 min after the mainshock (Fig. 2a).

The core is surrounded by a zone of enhanced seismicity ('corona') whose rate increased over the background by a factor of two to five, in an area five to ten times larger than the core. The corona appears immediately; its extent 2d after the mainshock is only slightly smaller than 5 yr later (Extended Data Fig. 2a,b). There were $22\ M_{\rm JMA}\!\ge\!6.7$ earthquakes (JMA, Japan Meteorological Agency) in the corona during the decade after the mainshock, but only four or five in the same area in the decade beforehand, so the corona is a robust feature not just for $M\!\ge\!3$ shocks, but for large, damaging ones as well.

A cross-section through the rupture shows that the core and corona extend throughout the lithosphere, to a depth of at least 50 km (Fig. 3a). The Coulomb stress change imparted by the mainshock to aftershock focal mechanisms indicates that most of the

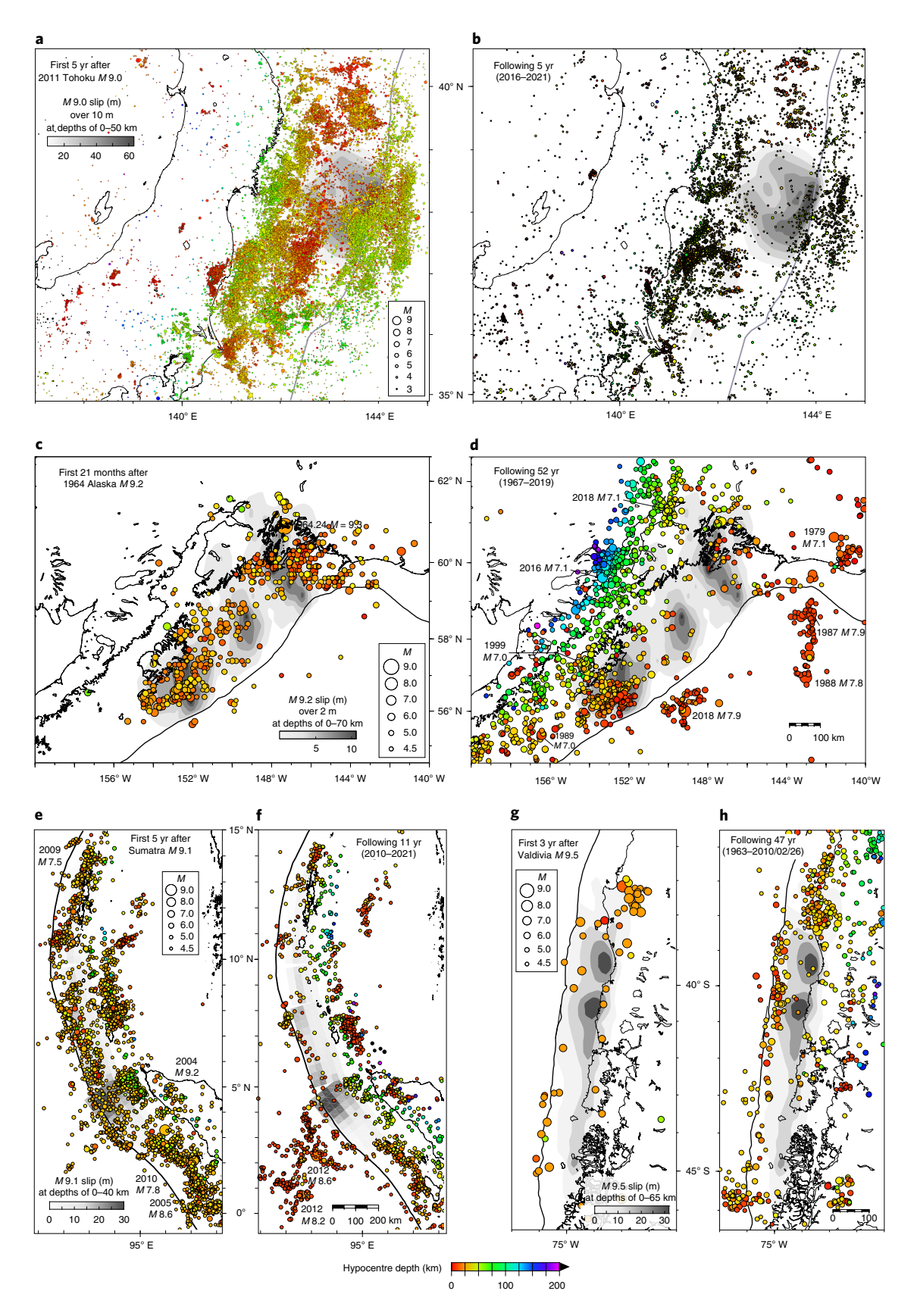


Fig. 1 Aftershocks of $M \ge 9.0$ megathrust ruptures since 1960. a,b, 2011 Tohoku: $M \ge 3.0$ shocks from JMA; slip from ref. ¹⁹. c,d, 1964 Prince William Sound: $M \ge 4.5$ shocks from ref. ⁴³ for first 21 months, and from the Advanced National Seismic System (ANSS) afterwards; slip from ref. ⁴⁴. e,f, 2004 Sumatra: $M \ge 4.5$ shocks from ANSS, with $M \ge 7.0$ events labelled; slip from ref. ⁴⁵. g,h, 1960 Valdivia: $M \ge 4.5$ shocks from ANSS; slip from ref. ²⁴, with three isolated patches of slip below 75 km, probably numerical artefacts, not shown. Seismicity on the rupture surface shut down within 5 yr, whereas seismicity in the surrounding corona lasts up to 50 yr. In each case, we plot seismicity near or above the magnitude of completeness for the period shown.

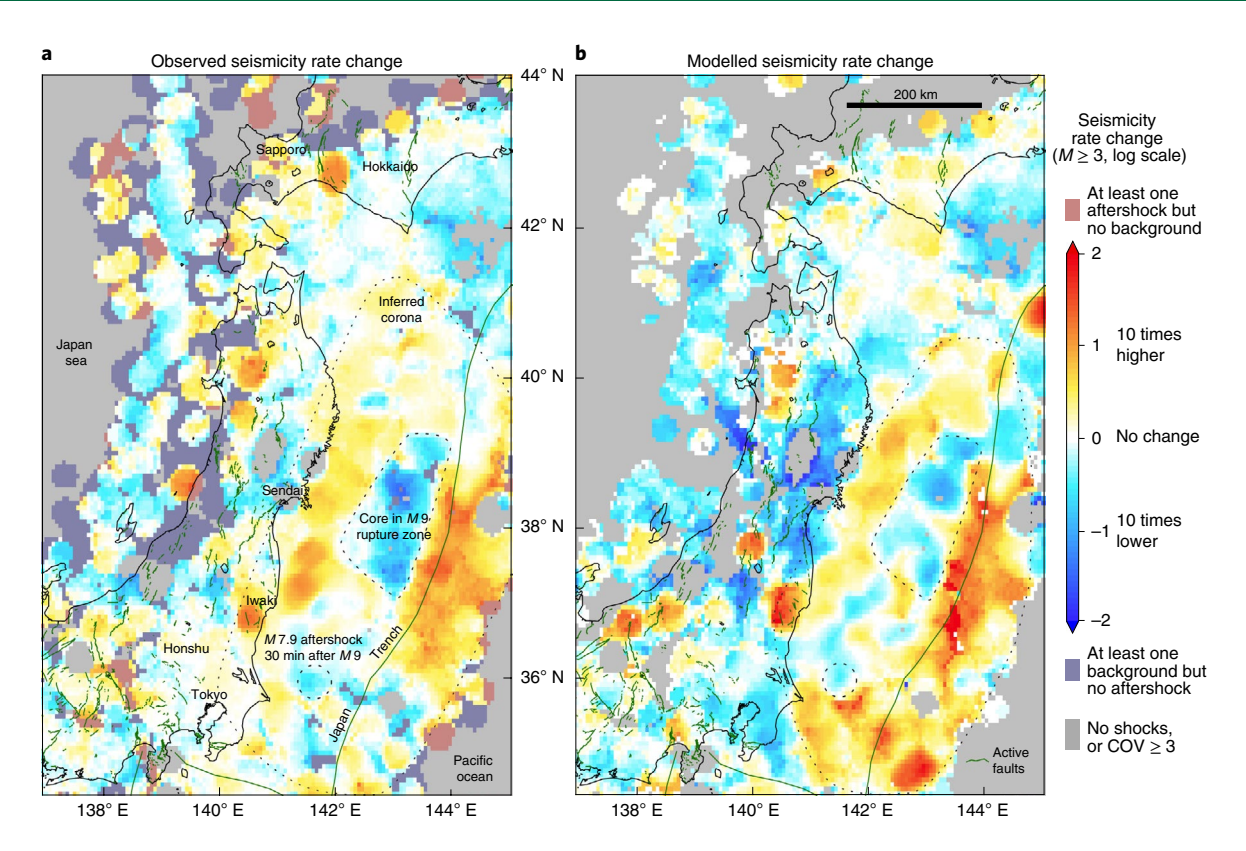


Fig. 2 | Change in seismicity rate beginning 5 yr after the Tohoku M9 earthquake. The seismicity 5-10 yr after the mainshock is compared with 13 yr before the M9 (11 March 2016-11 March 2021 / 1 January 1998-11 March 2011 14:45), for <150 km depth and a 20 km smoothing radius. **a**, Observed rate change. The 'core', in which the seismicity has shut down, collocates with the rupture^{19,46}. The surrounding corona has been the site of 22 $M \ge 6.7$ shocks since the M9 struck. Aftershock zones and swarms during the pre-mainshock period are masked where coefficient of variation (COV) ≥ 3, as explained in Methods. Active faults are green. **b**, The rate-state Coulomb model resembles the observed seismicity-rate changes, with a spatial regression coefficient of 0.61 and a slope of 0.67.

aftershocks were brought closer to Coulomb failure (Fig. 3b) by the mainshock, suggesting that the corona is a product of stress transfer from the core to surrounding faults²⁰. The stress imparted to the aftershocks is largely positive (Fig. 3b), promoting failure, whereas stress imparted to the background (pre-*M*9) mechanisms is largely negative (Fig. 3c), inhibiting failure. This means that a different set of faults was activated by the mainshock than beforehand. This is possible because there are diverse mechanisms in the descending Pacific plate, the overlying forearc (distance <100 km) and the outer rise (distance >175 km in Fig. 3b).

Though smaller, the 2003 M8.2 Tokachi-oki earthquake also exhibits a core shutdown and corona activation (Extended Data Fig. 3b). Like Tohoku, the Tokachi-oki core resembles the high-slip zone, the core shuts down by a factor of three to five below the background rate, and the rate of corona seismicity is three to five times higher than the background rate. Although network detection for the 2010 M8.8 Maule aftershocks is much poorer, a core and corona are possible there, too (Extended Data Fig. 3a).

Forecasting these seismicity changes from Coulomb stress transfer

The theory of rate and state friction²¹ coupled with Coulomb stress transfer^{15,16} provides a framework for interpreting these observations, and for forecasting future seismicity. In rate–state friction under conditions of constant tectonic loading, Coulomb stress increases amplify the background seismicity rate, and stress decreases diminish it, with both effects decaying with time. Areas with a high background seismicity rate thus respond to small stress changes, whereas in areas with low seismicity rates the stress changes have little effect.

We use earthquake focal mechanisms as proxies for active faults in an attempt to capture their complexity and heterogeneity 22 . We tune the model by adjusting the background rates so that the predicted seismicity changes caused by the Tohoku mainshock and all $M \ge 6.5$ aftershocks that struck during the first 5 yr match the observations (Methods). The forecast resembles the observed seismicity, capturing the core and the corona, with a spatial regression coefficient 0.61 and a regression slope of 0.67 for the 14,433 non-zero 0.06° cells.

The time evolution of seismicity in the core and corona can be generalized by a mean stress increase in the corona and a mean stress decrease in the core (Fig. 4). To capture the heterogeneity of source fault slip and the diversity of receiver fault geometries²³, we use Monte Carlo simulation, represented here by the s.d. of the stress change (Extended Data Fig. 4 gives the full suite of realizations). Even though the mean stress drops in the core, with a sufficiently large s.d. some core faults receive a stress increase, causing a sudden seismicity rate increase (Extended Data Fig. 1c). However, these sites are rapidly consumed, resulting in a delayed shutdown. A much briefer delayed shutdown was seen in a lobe of calculated stress decrease of the 1992 M7.3 Landers earthquake¹⁷. The generalized seismicity time histories in Fig. 4 resemble the observations. If the stress drop in the M9.5 earthquake were $\sim 50\%$ larger than the others^{20,24}, its behaviour²⁵ would also match the generalized curves. The model has elements in common with the Scholz seismicity spacetime diagram²⁶ (Extended Data Fig. 4e), and with the Mogi doughnut^{27,28}, although we regard the core and corona as postseismic rather than precursory phenomena.

Our model omits several processes that could modify the curves in Fig. 4. Dynamic stress triggering could elevate the aftershock

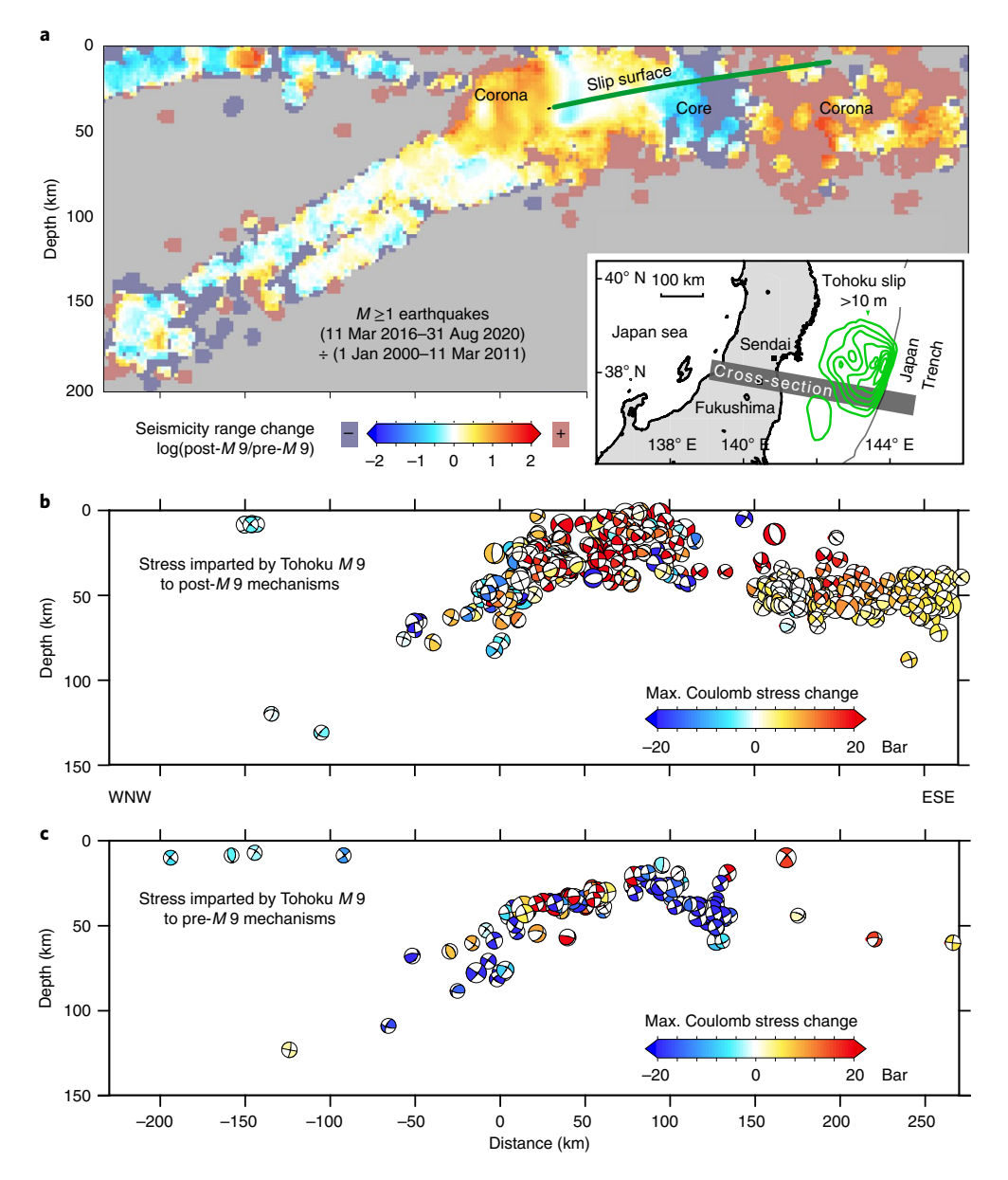


Fig. 3 | Cross-sections of seismicity-rate and stress change for the Tohoku M9 earthquake. a, Seismicity-rate change as in Fig. 2a, showing that the core and corona extend through the lithosphere. **b**, Coulomb stress change resolved onto aftershock focal mechanisms (side projections, with the most recent shocks plotted on top). Most nodal planes were brought closer to failure by the mainshock, activating these faults, probably causing the corona aftershocks in **a. c**, Background mechanisms are brought farther from failure, inactivating these faults. The diversity of receiver faults leads to heterogeneity of the stress transfer. Assumed fault friction is 0.4, with mechanisms coloured by the most positively stressed nodal plane. If the outer rise shocks were shallower, as suggested by an ocean bottom seismometer network⁴⁷, they would be even more strongly promoted.

rate in both the core and corona, particularly in the first ~10 d (ref. ²⁹). Viscoelastic relaxation probably intensifies and prolongs the corona, because coseismic tractions exerted at the base of the crust broaden the stress distribution during the first few decades^{30,31}. Postseismic creep, which like seismicity is driven by stress transfer from the rupture, probably contributes to the corona, but not to the core (Extended Data Fig. 3). For Tohoku³² and Sumatra³³, postseismic creep occurs only in the corona, and is small and patchy, with a magnitude of ~3% of the coseismic slip; for Maule, creep occurred downdip of the core with ~10% of the coseismic slip; for Tokachi, postseismic creep occurred throughout the corona at ~15% of the coseismic slip³⁴, and so plays a larger role. Since only negligible creep is detected in the cores of these earthquakes, the temporal transition from aftershocks to shutdown is probably unrelated to creep.

Because the corona is evident within 2 d of the Tohoku shock, and grows only by about 10% in the next several months, it cannot be principally caused by afterslip or relaxation. If it were caused by dynamic stress, it would probably shrink after the first 10 d or so, which is not seen. Thus, static stress transfer seems the best explanation for its existence.

Persistence of the core shutdown and corona seismicity

We attribute the conflicting megathrust aftershock observations in the literature principally to the different time periods and locations relative to the mainshock in which aftershocks were analysed. As a result, the transition from abundant aftershocks on the rupture surface to its shutdown was missed. Because the corona is as much as ten times the area of the core, there is a net hazard increase after

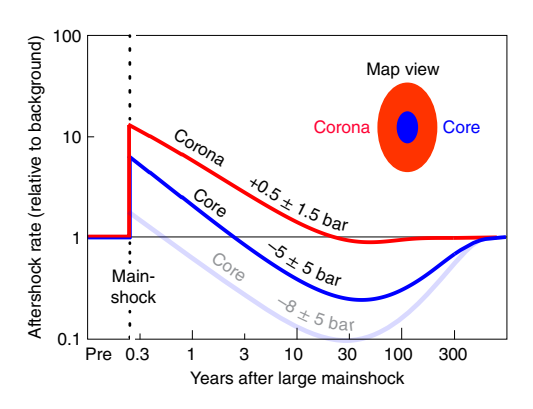


Fig. 4 | Modelled response of seismicity to a megathrust earthquake.

In the corona (red curve), the seismicity rate jumps and then decays to the background rate over ~40 yr. In the core (dark-blue curve), the rate also jumps, but decays within a few years below its pre-mainshock level, where it remains for centuries. The stress-change s.d. values are used to represent the heterogeneity of the imparted stress. $t_{\rm a}$ is 20 yr, $A\sigma$ is 0.5 bar and the curves are means of Monte Carlo simulations. A larger stress drop in the core (light-blue curve) causes a more rapid shutdown, perhaps explaining the 1960 M 9.5 aftershocks.

a megathrust that lasts for about half a century, typically spanning the outer rise to the coast. Megathrust aftershock zones, even when measured in the first few days, greatly overestimate their rupture areas^{10,35}. Instead, the core area that emerges several years after the mainshock best corresponds to the primary rupture zone. Since the core is forecast to remain shut down for periods roughly corresponding to megaquake interevent times, the core shutdown has some resemblance to the seismic gap hypothesis³⁶. However, in the gap hypothesis, the hazard drops with the occurrence of the mainshock, opposite to what we find.

Our result may explain a 20-year-old enigma for large worldwide shocks¹¹. By stacking over 100 *M*≥7 mainshocks, Parsons found an aftershock duration of 10 or more years on faults that received a calculated shear stress increase, but only one year on faults that received a shear stress decrease. Parsons proposed that aftershocks on faults with stress decreases could be caused by dynamic triggering. However, these results could also be explained by our model: the stress decreases occur close to the mainshocks, at ~50 km from the centroids, while the stress increases occur ~75 km from the centroids. Therefore, the 1 yr aftershocks might lie principally in the core, with the 10 yr aftershocks in the corona. Our generalized curves and Parsons's observations are juxtaposed in Extended Data Fig. 5.

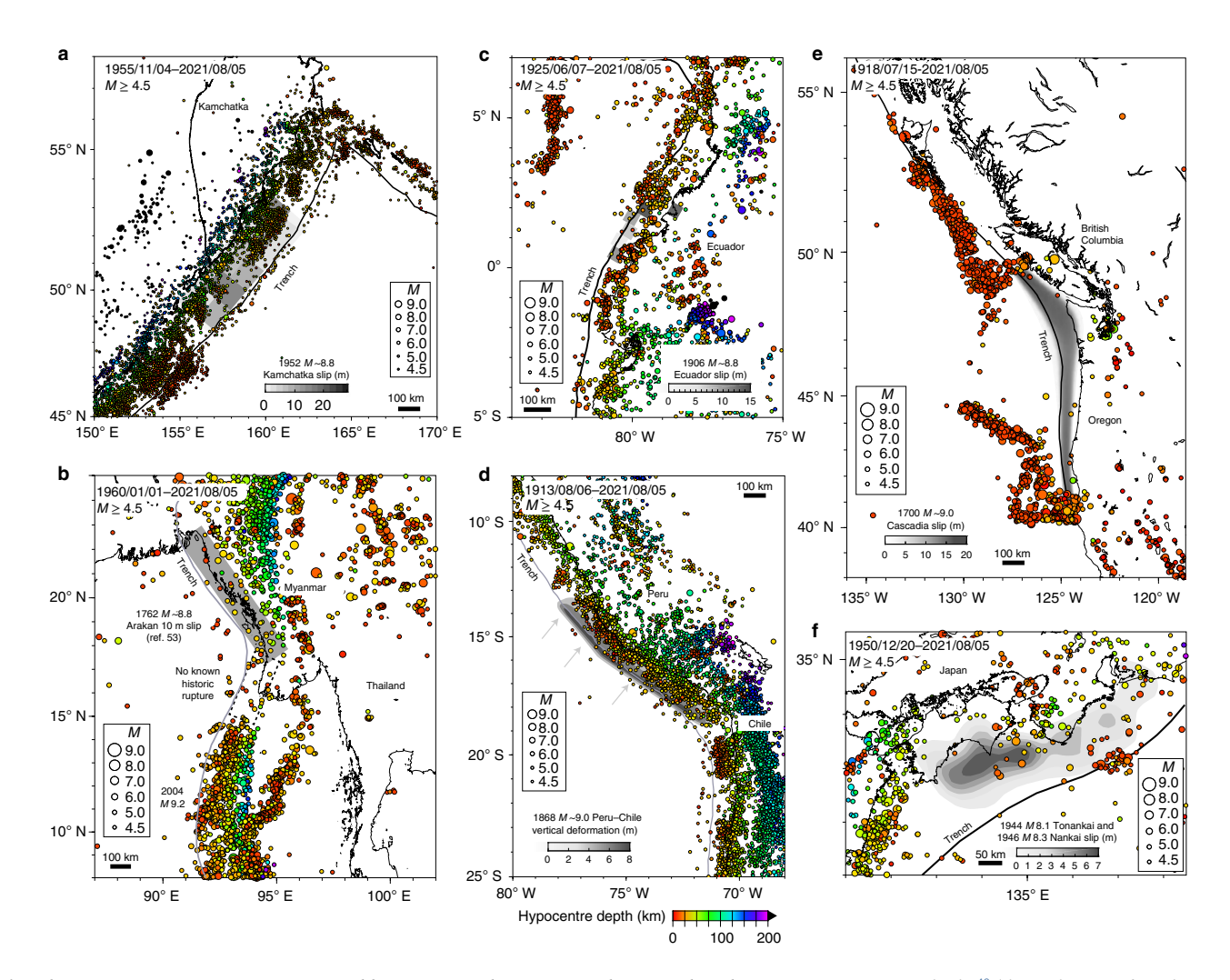


Fig. 5 | Contemporary gaps in seismicity could represent prehistoric megathrust earthquakes. a, 1952 *M* -8.8 Kamchatka⁴⁸ (the authors' preferred 'JASmod7' model shown). **b**, 1762 *M* -8.8 Arakan⁴⁹. **c**, 1906 *M* -8.8 Ecuador⁵⁰. **d**, 1868 *M* -9.0 Arica, Peru-Chile⁵¹ with several holes (arrows) seen along the modelled uniform-slip rupture. **e**, 1700 *M* -9.0 Cascadia⁵². **f**, 1944 M 8.1 Tonankai and 1946 M 8.3 Nankai⁵³. ANSS seismicity.

The agreement between the observed and modelled seismicity-rate changes in Fig. 2 for a 5 yr retrospective forecast period suggests that the rate–state Coulomb model exhibits forecast ability that could enhance hazard assessments. For example, four $M \sim 7$ earth-quakes struck along the Tohoku coast in 2021–2022, all in corona areas of high forecast likelihood (Extended Data Fig. 1a). The seismicity rate at these epicentres has been undergoing an Omori decay since the M9, with a rate approximately five times higher in 2021 than the pre-M9 background rate³⁷. This suggests that the $M \sim 7$ events are corona aftershocks.

The expected multicentury persistence of the core, if true, would mean that sites of preinstrumental and prehistoric megathrust earthquakes appear as 'holes' in subduction seismicity. All four of the megathrusts in Fig. 1 are visible today as seismicity holes (Extended Data Fig. 6). While holes might also result from creeping portions of subduction zones, creep is most often accompanied by seismicity rather than its absence³⁸. Holes at or near the sites of coseismic slip are evident to various degrees for the still older 1952 M~8.8 Kamchatka, 1946 M8.3 Nankai, 1944 M8.1 Tonankai, 1906 $M \sim 8.8$ Ecuador, 1868 $M \sim 9.0$ Arica (Peru-Chile), 1762 $M \sim 8.8$ Arakan (Myanmar) and 1700 $M \sim 9.0$ Cascadia earthquakes (Fig. 5). While the lack of Cascadia seismicity has been attributed to complete healing and locking of the megathrust³⁹, its low seismicity rate and low aftershock productivity⁴⁰ suggest that it could still be in a post-mainshock shutdown. Candidate prehistoric megathrust ruptures include a 700-km-long seismicity hole along the Commander section of the northwest Aleutian arc41, and a 300-km-long hole along the western Makran Trench⁴² (Extended Data Fig. 9). Seismicity holes might also mark the sites of historic $M \sim 8$ transform fault ruptures, such as the 1857 and 1906 San Andreas earthquakes²⁶.

Online content

Any methods, additional references, Nature Research reporting summaries, source data, extended data, supplementary information, acknowledgements, peer review information; details of author contributions and competing interests; and statements of data and code availability are available at https://doi.org/10.1038/s41561-022-00954-x.

Received: 19 October 2021; Accepted: 27 April 2022;

Published online: 10 June 2022

References

- Ryder, I. et al. Large extensional aftershocks in the continental forearc triggered by the 2010 Maule earthquake, Chile. Geophys. J. Int. 188, 879–890 (2012).
- 2. Kato, A. & Igarashi, T. Regional extent of the large coseismic slip zone of the 2011 $M_{\rm w}$ 9.0 Tohoku-oki earthquake delineated by on-fault aftershocks. *Geophys. Res. Lett.* **39**, L15301 (2012).
- Henry, C. & Das, S. Aftershock zones of large shallow earthquakes: fault dimensions, aftershock area expansion and scaling relations. *Geophys. J. Int.* 147, 272–293 (2001).
- Kanamori, H. Rupture processes of subduction-zone. Annu. Rev. Earth Planet Sci. 14, 293–322 (1986).
- Rietbrock, A. et al. Aftershock seismicity of the 2010 Maule M_w=8.8, Chile, earthquake: correlation between co-seismic slip models and aftershock distribution? *Geophys. Res. Lett.* 39, L08310 (2012).
- Bilek, S. L. & Lay, T. Subduction zone megathrust earthquakes. Geosphere 14, 1468–1500 (2018).
- Lengliné, O., Enescu, B., Peng, Z. & Shiomi, K. Decay and expansion of the early aftershock activity following the 2011, M_w9.0 Tohoku earthquake. Geophys. Res. Lett. 39, L18309 (2012).
- Thatcher, W. Order and diversity in the modes of circum-Pacific earthquake recurrence. J. Geophys. Res. 95, 2609–2623 (1990).
- Woessner, J., Schorlemmer, D., Wiemer, S. & Mai, P. M. Spatial correlation of aftershock locations and on-fault main shock properties. *J. Geophys. Res.* 111, B08301 (2006).
- Wetzler, N., Lay, T., Brodsky, E. E. & Kanamori, H. Systematic deficiency of aftershocks in areas of high coseismic slip for large subduction zone earthquakes. Sci. Adv. 4, eaao3225 (2018).
- Parsons, T. Global Omori law decay of triggered earthquakes: large aftershocks outside the classical aftershock zone. J. Geophys. Res. 107, 2199 (2002).

- Hainzl, S., Christophersen, A., Rhoades, D. & Harte, D. Statistical estimation of the duration of aftershock sequences. *Geophys. J. Int.* 205, 1180–1189 (2016).
- Lay, T., Astiz, L., Kanamori, H. & Christensen, D. H. Temporal variation of large intraplate earthquakes in coupled subduction zones. *Phys. Earth Planet. Int.* 54, 258–312 (1989).
- Ogata, Y. Space-time point-process models for earthquake occurrences. Ann. Inst. Stat. Math. 50, 379–402 (1998).
- Stein, R. S. The role of stress transfer in earthquake occurrence. Nature 402, 605–609 (1999).
- Harris, R. A. & Simpson, R. W. Suppression of large earthquakes by stress shadows: a comparison of Coulomb and rate-and-state failure. *J. Geophys. Res.* 103, 24439–24451 (1998).
- Toda, S., Stein, R. S., Beroza, G. & Marsan, D. Aftershocks halted by static stress shadows. *Nat. Geosci.* 5, 410–413 (2012).
- Woessner, J. & Wiemer, S. Assessing the quality of earthquake catalogues: estimating the magnitude of completeness and its uncertainty. *Bull. Seismol. Soc. Am.* 95, 684–698 (2005).
- Iinuma, T. et al. Coseismic slip distribution of the 2011 off the Pacific Coast of Tohoku Earthquake (M9.0) refined by means of seafloor geodetic data. J. Geophys. Res. 117, B07409 (2012).
- Lin, J. & Stein, R. S. Stress triggering in thrust and subduction earthquakes and stress interaction between the southern San Andreas and nearby thrust and strike-slip faults. J. Geophys. Res. 109, B02303 (2004).
- Dieterich, J. H. A constitutive law for the rate of earthquake production and its application to earthquake clustering. J. Geophys. Res. 99, 2601–2618 (1994).
- Hardebeck, J. L., Nazareth, J. J. & Hauksson, E. The static stress change triggering model: constraints from two southern California aftershock sequences. J. Geophys. Res. 103, 24427–24437 (1998).
- Helmstetter, A. & Shaw, B. E. Relation between stress heterogeneity and aftershock rate in the rate-and-state model. J. Geophys. Res. 111, B07304 (2006).
- Barrientos, S. E. & Ward, S. N. The 1960 Chile earthquake: inversion for slip distribution from surface deformation. *Geophys. J. Int.* 103, 589–598 (1990).
- Cifuentes, I. L. The 1960 Chilean earthquakes. J. Geophys. Res. 94, 665–680 (1989).
- Scholz, C. H. Mechanisms of seismic quiescences. Pure Appl. Geophys. 126, 701–718 (1988).
- Mogi, K. Some features of recent seismic activity in and near Japan (2) Activity before and after great earthquakes. Bull. Earthq. Res. Inst. 47, 395–417 (1969).
- Schurr, B. et al. Forming a Mogi doughnut in the years prior to and immediately before the 2014 M8.1 Iquique, northern Chile earthquake. Geophys. Res. Lett. 47, e2020GL088351 (2020).
- Pollitz, F. F., Stein, R. S., Sevilgen, V. & Bürgmann, R. The 11 April 2012 east Indian Ocean earthquake triggered large aftershocks worldwide. *Nature* 490, 250–253 (2012).
- Freed, A. M. & Lin, J. Accelerated stress buildup on the southern San Andreas fault and surrounding regions caused by Mojave Desert earthquakes. *Geology* 30, 571–574 (2002).
- Bürgmann, R., Uchida, N., Hu, Y. & Matsuzawa, T. Tohoku rupture reloaded? Nat. Geosci. 9, 183 (2016).
- Iinuma, T. et al. Seafloor observations indicate spatial separation of coseismic and postseismic slips in the 2011 Tohoku earthquake. *Nat. Commun.* 7, 13506 (2016).
- Hu, Y. & Wang, T. Spherical-earth finite element model of short-term postseismic deformation following the 2004 Sumatra earthquake. J. Geophys. Res. 117, B0504 (2012).
- Baba, T., Hirata, K., Hori & Sakaguchi, H. Offshore geodetic data conducive to the estimation of the afterslip distribution following the 2003 Tokachi-oki earthquake. Earth Planet. Sci. Lett. 241, 281–292 (2006).
- Neo, J. C., Huang, Y., Yao, D. & Wei, S. Is the aftershock zone area a good proxy for the mainshock rupture area? *Bull. Seismol. Soc. Am.* 111, 424–438 (2020).
- McCann W. R., Nishenko S. P., Sykes L. R. & Krause, J. in Earthquake Prediction and Seismicity Patterns. Contributions to Current Research in Geophysics (ed. Wyss, M.) 1082-1147 (Birkhäuser, 1979).
- Toda, S. & Stein, R. S. Recent large Japan quakes are aftershocks of the 2011 Tohoku earthquake. *Temblor* https://doi.org/10.32858/temblor.175 (2021).
- Wang, K. & Bilek, S. L. Invited review paper: Fault creep caused by subduction of rough seafloor relief. *Tectonophysics* 610, 1–24 (2014).
- Obana, K. et al. Earthquake activity in northern Cascadia subduction zone off Vancouver Island revealed by ocean-bottom seismograph observations. *Bull. Seismol. Soc. Am.* 105, 489–495 (2014).
- Gomberg, J. & Bodin, P. The productivity of Cascadia aftershock sequences. Bull. Seismol. Soc. Am. 111, 1494–1507 (2021).
- Lutikov, A. I., Rogozhin, E. A., Dontsova, G., Yu & Zhukovets, V. N. The M_w7.8 earthquake of July 17, 2017 off the Commander Islands and other large earthquakes at the western segment of the Aleutian Island Arc. *J. Volcanol. Seismol.* 13, 112–123 (2019).
- Okal, E. A. & Synolakis, C. E. Far-field tsunami hazard from mega-thrust earthquakes in the Indian Ocean. *Geophys. J. Int.* 172, 995–1015 (2008).

- 43. Page, R. Aftershocks and microaftershocks of the great Alaska earthquake of 1964. *Bull. Seismol. Soc. Am.* **58**, 1131–1168 (1968).
- Ichinose, G., Somerville, P., Thio, H. K., Graves, R. & O'Connell, D. Rupture process of the 1964 Prince William Sound, Alaska, earthquake from the combined inversion of seismic, tsunami, and geodetic data. *J. Geophys. Res.* 112, B07306 (2007).
- Banerjee, P., Pollitz, F., Nagarajan, B. & Bürgmann, R. Coseismic slip distributions of the 26 December 2004 Sumatra–Andaman and 28 March 2005 Nias earthquakes from GPS static offsets. *Bull. Seismol. Soc. Am.* 97, S86–S102 (2007).
- 46. Tajima, F., Mori, J. & Kennett, B. L. N. A review of the 2011 Tohoku-oki earthquake ($M_{\rm w}$ 9.0): large-scale rupture across heterogeneous plate coupling. *Tectonophysics* **586**, 15–34 (2013).
- Obana, K. et al. Seismic velocity structure and its implications for oceanic mantle hydration in the trench—outer rise of the Japan Trench. *Geophys. J. Int.* 217, 1629–1642 (2019).
- MacInnes, B. T., Weiss, R., Bourgeois, J. & Pinegina, T. K. Slip distribution of the 1952 Kamchatka great earthquake based on near-field tsunami deposits and historical records. *Bull. Seismol. Soc. Am.* 100, 1695–1709 (2010).

- Cummins, P. R. The potential for giant tsunamigenic earthquakes in the northern Bay of Bengal. *Nature* 449, 75–78 (2007).
- Yoshimoto, M. et al. Depth-dependent rupture mode along the Ecuador-Colombia subduction zone. *Geophys. Res. Lett.* 44, 2203–2210 (2017).
- Okal, E. A., Borrero, J. C. & Synolakis, C. E. Evaluation of tsunami risk from regional earthquakes at Pisco, Peru. *Bull. Seismol. Soc. Am.* 96, 1634–1648 (2006).
- 52. Wang, K. & Trehu, A. M. Invited review paper: Some outstanding issues in the study of great megathrust earthquakes—the Cascadia example. *J. Geodyn.* **98**, 1–18 (2016).
- Sagiya, T. & Thatcher, W. Coseismic slip resolution along a plate boundary megathrust: the Nankai Trough, southwest Japan. *J. Geophys. Res.* 104, 1111–1129 (1999).

Publisher's note Springer Nature remains neutral with regard to jurisdictional claims in published maps and institutional affiliations.

© The Author(s), under exclusive licence to Springer Nature Limited 2022

Methods

Observed seismicity rate change. We employ two methods to enhance the representation of seismicity rate change in Fig. 2 (map view) and Fig. 3a (cross-section). To quantify a rate change in a cell, there must be at least one earthquake in the background (pre-mainshock) period, and at least one in the post-mainshock period. However, there are many cells where this condition is not met. Therefore, if there are earthquakes in the post-mainshock period but none in the background period, we use a muted red colour to represent an unquantifiable increase. For an unquantifiable decrease, we use a muted blue colour. These cells are not used in the spatial regression of the observed on modelled rate changes.

A second complicating factor in the rate-change map is aftershock zones or seismic swarms that took place during the background period, which appear as blue discs in Extended Data Fig. 7a because they had abnormally high rates before the mainshock. These are unrelated to the impact of the subsequent Tohoku mainshock on seismicity. To mask these effects, we calculate the COV of the interevent times of the background seismicity in every cell. Typical stable background seismicity has $COV \approx 1$, whereas seismic swarms and aftershock sequences exhibit $COV \geq 3$, as shown in Extended Data Fig. 7b. Therefore, we mask areas with $COV \geq 3$ (Extended Data Fig. 7c) in Fig. 2b and Fig. 3a. Masked areas appear neutral grey and are identified as such.

Maximum Coulomb stress change imparted to focal mechanisms. We calculate the stress imparted to focal mechanisms in Fig. 2b, as illustrated in Fig. 3c,d and Extended Data Fig. 8a, rather than to mapped faults, idealized planar faults or optimally oriented faults. Although the faults on which such earthquakes strike can be small ($M \ge 3.0$ for Tohoku), we believe that these mechanisms provide a richer and more realistic indication of the distribution, geometry and rake of active faults, and so more faithfully capture their true complexity. Even nominally straight, isolated and high-slip-rate faults exhibit astonishing complexity when viewed by their focal mechanisms, by double-difference relocated seismicity or by seismic reflection. This complexity has many roots, including diverse fault orientations caused by the stress evolving over geologic time; by fault bends, breaks and junctions; by fault obliquity to the plate motion and by contrasting crustal properties and the presence of crustal fluids.

Although focal mechanisms may better reflect the three-dimensional and fractal nature of fault networks than do simple continuous surfaces, for non-zero fault friction there is nodal plane ambiguity because the Coulomb stress is not the same on the two planes of each mechanism. Therefore, here we assume a 0.4 friction coefficient 15 and report the stress change on the plane on which the Coulomb stress is most positive, which we refer to as the maximum Coulomb stress change. Since stress increases are coloured red, this introduces a 'red' bias, which carries two intrinsic benefits. The first is that calculation of seismicity-rate change, with which the stress changes are compared in Fig. 3, is also red biased, because it is easier to measure a seismicity-rate increase than a decrease, as one can only measure rate decreases if there are a sufficient number of quakes in the pre-mainshock period. The second benefit is that, by using the plane with the most positive stress change, focal mechanisms with stress decreases ('blue beachballs') must lie in the stress shadow; the stress decrease cannot be an artefact of nodal-plane selection. Thus, the predominance of blue beachballs in Fig. 3c means that the background fault population was indeed inactivated by the mainshock stress; these faults were shut down.

Forecast seismicity rate change. For the retrospective forecast shown in Fig. 2b, we use finite fault models for the mainshock rupture and the $M \ge 6.5$ earthquakes that struck during the first 5 yr after the mainshock (Extended Data Fig. 8b) as the source for the imparted stress, or if finite fault models are not available the most plausible rectangular fault using the empirical relations for the receiver faults, the planes on which we resolve the imparted stress, we use focal mechanisms of background shocks as proxies for active faults, calculating the imparted stress at their hypocentres. NIED (National Research Institute for Earth Science and Disaster Resilience) F-net provides focal mechanisms for $M \ge 3.0$ events in Japan. However, even for the dense Japanese seismic network, the distribution of focal mechanisms is relatively sparse. Therefore, we densify the data with 'synthetic' focal mechanisms in this manner: for shocks without a mechanism, we assign the closest mechanism, which acts to both densify and smooth the receiver faults.

In addition to the background seismicity rate, focal mechanisms and main shock finite fault models, in the seismicity-rate equation 21 the earthquake forecasts depend on three parameters: the after shock duration (the time until the quake rate decays back to the pre-main shock rate) $t_{\rm w}$, a constitutive parameter multiplied by the effective normal stress $A\sigma$, and the tectonic stressing rate τ . These parameters have the following relation:

$$t_{\rm a} = \frac{A\sigma}{\dot{\tau}}.\tag{1}$$

At least two parameters are required to implement rate–state formulations. Here we assume t_a = 20 yr, implying an interevent time of ~1,000 yr, roughly typical of megaquakes, and $A\sigma$ = 0.5 bar, which was found by fitting the observed number of aftershocks to the forecast number. Although the rate–state parameters (t_a and $A\sigma$) are probably heterogeneous, we take them to be uniform, a simplification.

In rate–state friction, large stress increases close to the rupture surface yield unrealistically high calculated seismicity rate immediately after the mainshock because of the exponential terms in the seismicity-rate equation. As a result, we would predict far too many near-fault aftershocks. To overcome this, we impose an arbitrary maximum stress change of 5 bar.

To incorporate successive stress changes imparted by multiple main shocks, we use the expression for seismicity rate, R, as a function of the state variable γ under a tectonic shear stressing rate $\dot{\tau}_r$ from ref. ²¹, as implemented in refs. ^{55,56}. Under constant shear stressing rate, the state variable reaches the steady state

$$\gamma_0 = \frac{1}{\dot{\tau}}.\tag{2}$$

In the absence of a stress perturbation, the seismicity rate is constant. R is then equivalent to the background rate r, because R is calculated from

$$R = \frac{r}{\gamma \dot{\tau}_r}. (3)$$

An earthquake imposes a sudden stress step Δ CFF (Coulomb failure function), and γ_{n-1} changes to a new value γ_n :

$$\gamma_n = \gamma_{n-1} \exp\left(\frac{-\Delta CFF}{A\sigma}\right). \tag{4}$$

To find the seismicity rate at the time of the stress step, we substitute the new state variable in equation (4). A stress increase on a fault causes γ to drop, so the fault slips at a higher rate, yielding a higher seismicity rate. Conversely, a sudden stress drop causes γ to jump, lowering the seismicity rate. The seismicity-rate change is transient and eventually recovers, corresponding to an evolution of γ , which for the next time step Δt is given by

$$\gamma_{n+1} = \left[\gamma_n - \frac{1}{\dot{\tau}_r} \right] \exp \left[\frac{-\Delta t \dot{\tau}_r}{A \sigma} \right] + \frac{1}{\dot{\tau}_r}.$$
(5)

The duration of the transient is inversely proportional to the fault stressing rate $\dot{\tau}_r$. The lower γ is at the time of a new stress jump, the more strongly the seismicity rate will be amplified.

To map the forecast seismicity rate, we smooth *R* with a vertical cylinder of radius 20 km at each grid point, and then calibrate the effect of the overlapping cylinders. The larger the radius, the smoother the map. To compare the modelled rate with the observed rate, we use the same smoothing radius for consistency.

To increase the fidelity of the forecasts, we use the first 5 yr as a learning period of this period compares the observed and forecast changes in seismicity rate of $M \ge 3$ earthquakes associated with the 16 $M \ge 6.5$ earthquake sources, including the $M \ge 0$ mainshock, during the period. The data—model misfit is then minimized by modifying the background rate for each calculation cell (see explanation in Fig. 10 in ref. 30). An alternative would be to vary t_a or $A\sigma$, but we found that correcting the background rate renders more stable results.

Modelled seismicity time series. The resulting stress changes on the background nodal planes imparted by the Tohoku earthquake are shown in Extended Data Fig. 2c,d. To simulate the time series of seismicity rate from such diverse stress changes on a group of heterogeneous receiver faults in rate-state friction (Fig. 4), we generate a pseudorandom normal distribution of Coulomb stress changes on 10,000 receiver faults arbitrarily assigned mean and s.d. We then compute the evolution of state variable at each nucleation following equations (4) and (5), and update the seismicity rate at each time step using equation (3). In Fig. 4, we show only the curve of the mean of all time histories associated with the 10,000 realizations, although there are a large range of rate curves in such Monte Carlo runs (Extended Data Fig. 4a). The s.d. values mimic the source and receiver fault diversity and the stress-change heterogeneity, which alters the time series of the mean curves. The effective Omori decay exponent increases with fault heterogeneity (and so with the resulting diversity of Coulomb stress changes), as shown in Extended Data Fig. 4c,d and in ref. 23. The steeper aftershock decay in the core than in the corona arises in the model from multiple adjacent stress increases in aftershocks, whereas aftershocks are more dispersed in the corona, and so fewer stress increases overlap.

Data availability

We used the USGS ANSS catalogue (https://earthquake.usgs.gov/earthquakes/search/), the JMA catalogue (https://www.data.jma.go.jp/svd/eqev/data/daily_map/index.html and https://www.data.jma.go.jp/svd/eqev/data/bulletin/eqdoc.html) and the NIED F-net focal mechanism catalogue (https://www.fnet.bosai.go.jp/event/search). We also used a published 1960 Chile earthquake catalogue²⁵, and a published 1960–1966 Alaska earthquake catalogue³³. All seismic slip ('finite fault') models are published and cited; those also available from http://equake-rc.info/SRCMOD/searchmodels/allevents/include the 2003 Tokachi-oki⁵⁷ and 2011 Tohoku⁵⁸ earthquakes (used for Coulomb calculations) and 1944 Tonankai⁵³, 1946 Nankai⁵³ and 2010 Maule⁵⁹ (used for display in figures). Seismic slip models

available only from publications include the 1700 $M \sim 9.0$ Cascadia⁵², 1762 $M \sim 8.8$ Arakan⁴⁹, 1868 $M \sim 9.0$ Arica, Peru–Chile⁵¹, 1906 $M \sim 8.8$ Ecuador⁵⁰, 1952 Kamchatka⁴⁸, 1960 Valdivia²⁴, 1964 Prince William Sound⁴⁴ and 2004 Sumatra⁴⁵ earthquakes. Source data are provided with this paper.

Code availability

The numerical methodology used in this study is described in Methods and in refs. 55,56. We used the Coulomb 3.3 software. (software, tutorial files and user guide accessible via http://www.temblor.net/coulomb). For magnitude of completeness and aftershock decay calculations, we used ZMAP¹⁸ (http://www.seismo.ethz.ch/en/research-and-teaching/products-software/software/ZMAP/ and https://github.com/swiss-seismological-service/zmap7).

References

- Wells, D. & Coppersmith, K. J. New empirical relationships among magnitude, rupture length, rupture width, rupture area, and surface displacement. *Bull. Seismol. Soc. Am.* 84, 974–1002 (1994).
- Toda, S., Stein, R. S., Richards-Dinger, K. & Bozkurt, S. B. Forecasting the evolution of seismicity in southern California: animations built on earthquake stress transfer. *J. Geophys. Res.* 110, B05S16 (2005).
- Toda, S. & Stein, R. S. Long- and short-term stress interaction of the 2019 Ridgecrest sequence and Coulomb-based earthquake forecasts. *Bull. Seismol. Soc. Am.* 110, 1765–1780 (2020).
- 57. Yagi, Y. Source rupture process of the 2003 Tokachi-oki earthquake determined by joint inversion of teleseismic body wave and strong ground motion data. *Earth Planets Space* **56**, 311–316 (2004).
- 58. Ide, S., Baltay, A. & Beroza, G. C. Shallow dynamic overshoot and energetic deep rupture in the 2011 $M_{\rm w}$ 9.0 Tohoku-oki earthquake. *Science* **332**, 1426–1429 (2011).
- Lorito, S. et al. Limited overlap between the seismic gap and coseismic slip of the great 2010 Chile earthquake. Nat. Geosci. 4, 173–177 (2011).
- Toda, S., Stein, R. S., Sevilgen, V. & Lin, J. Coulomb 3.3, Graphic-Rich Deformation and Stress Change Software for Earthquake, Tectonic, and Volcano Research and Teaching—User Guide Open-File Report 2011-1060 (USGS, 2011).

- Lin, Y.-N. N. et al. Coseismic and postseismic slip associated with the 2010 Maule earthquake, Chile: characterizing the Arauco Peninsula barrier effect. J. Geophys. Res. 118, 3142–3159 (2013).
- Lobkovsky, L. I. et al. The Komandor seismic gap: earthquake prediction and tsunami computation. Oceanology 54, 519–531 (2014).
- Byrne, D. E., Sykes, L. R. & Davis, D. M. Great thrust earthquakes and aseismic slip along the plate boundary of the Makran Subduction Zone. *J. Geophys. Res.* 97, 449–478 (1992).
- 64. Yeats, R. S. Active Faults of the World 332-334 (Cambridge Univ. Press, 2012).

Acknowledgements

We thank C. Scholz, T. Parsons and W. Thatcher for insightful comments on the manuscript. We gratefully acknowledge support from the SBIR programme of the US National Science Foundation (R.S.S.) and the WTW Research Network (R.S.S.). The funders were provided with the manuscript upon submission, but had no role in study design, data collection and analysis, decision to publish or preparation of the manuscript.

Author contributions

S.T. and R.S.S. contributed equally to the ideas, methods, text and figures in this study.

Competing interests

The authors declare no competing interests.

Additional information

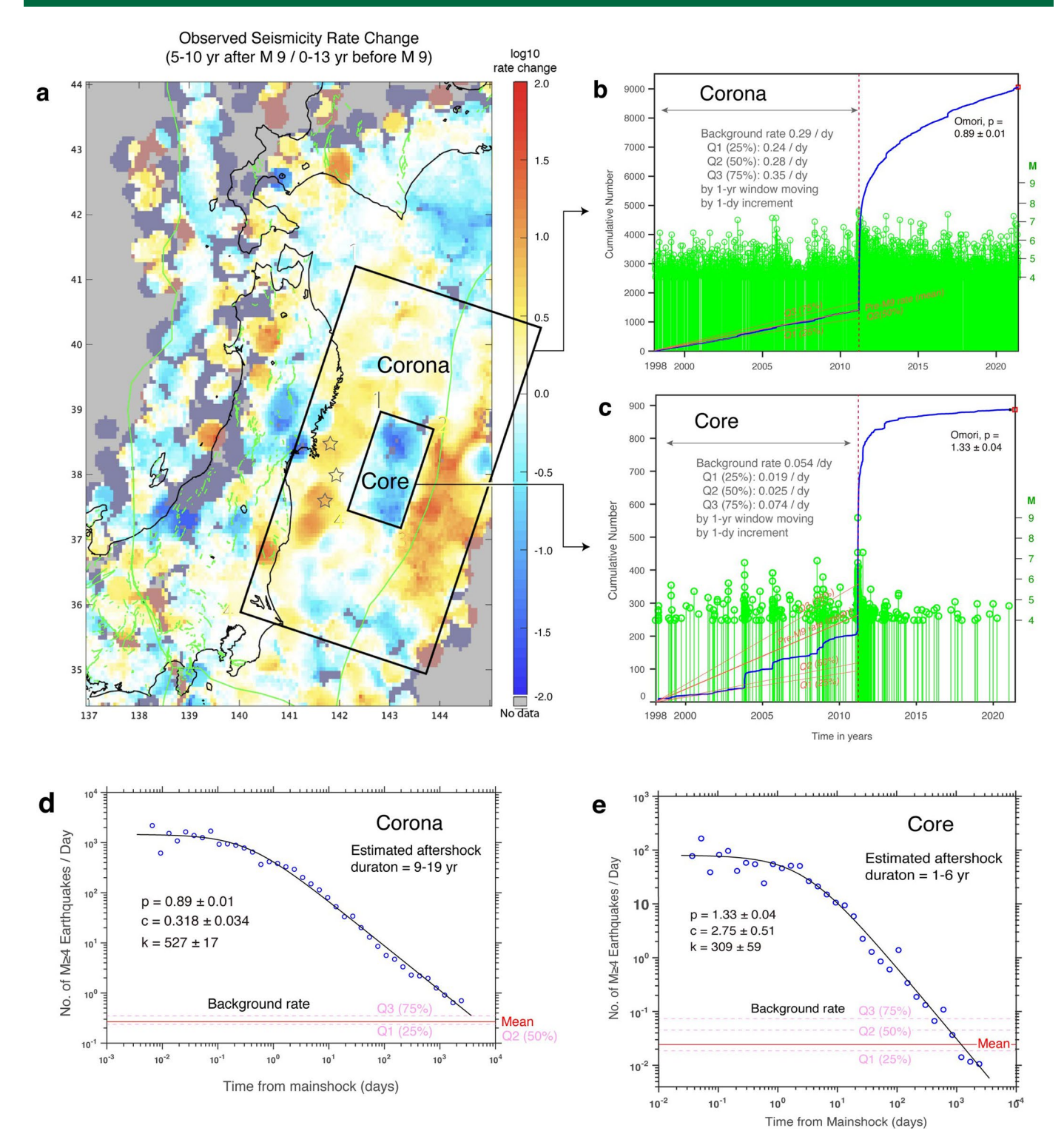
Extended data is available for this paper at https://doi.org/10.1038/s41561-022-00954-x.

Supplementary information The online version contains supplementary material available at https://doi.org/10.1038/s41561-022-00954-x.

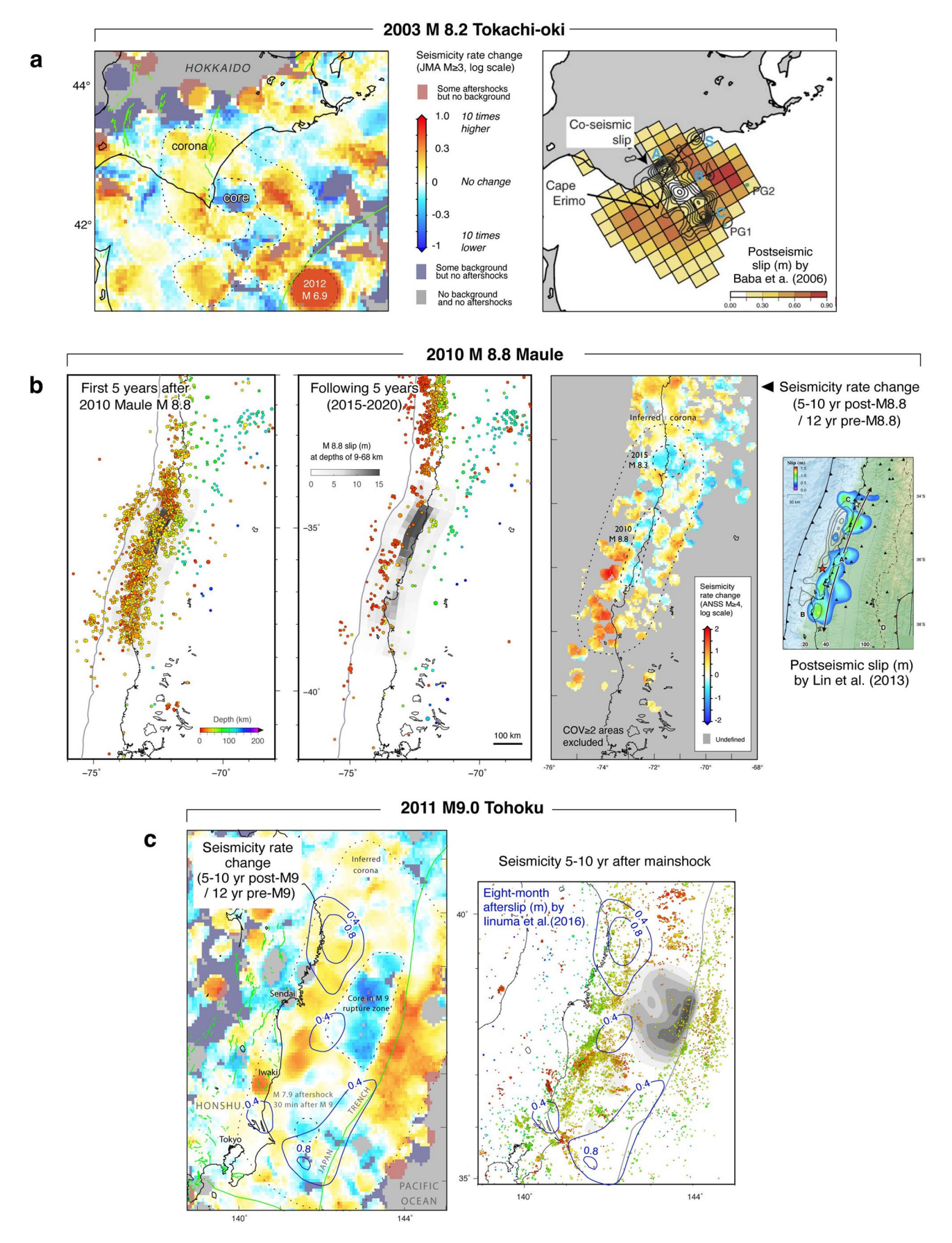
Correspondence and requests for materials should be addressed to Shinii Toda or Ross S. Stein.

Peer review information *Nature Geoscience* thanks Lingling Ye, Olaf Zielke and the other, anonymous, reviewer(s) for their contribution to the peer review of this work. Primary Handling Editor: Louise Hawkins, in collaboration with the *Nature Geoscience* team.

Reprints and permissions information is available at www.nature.com/reprints.

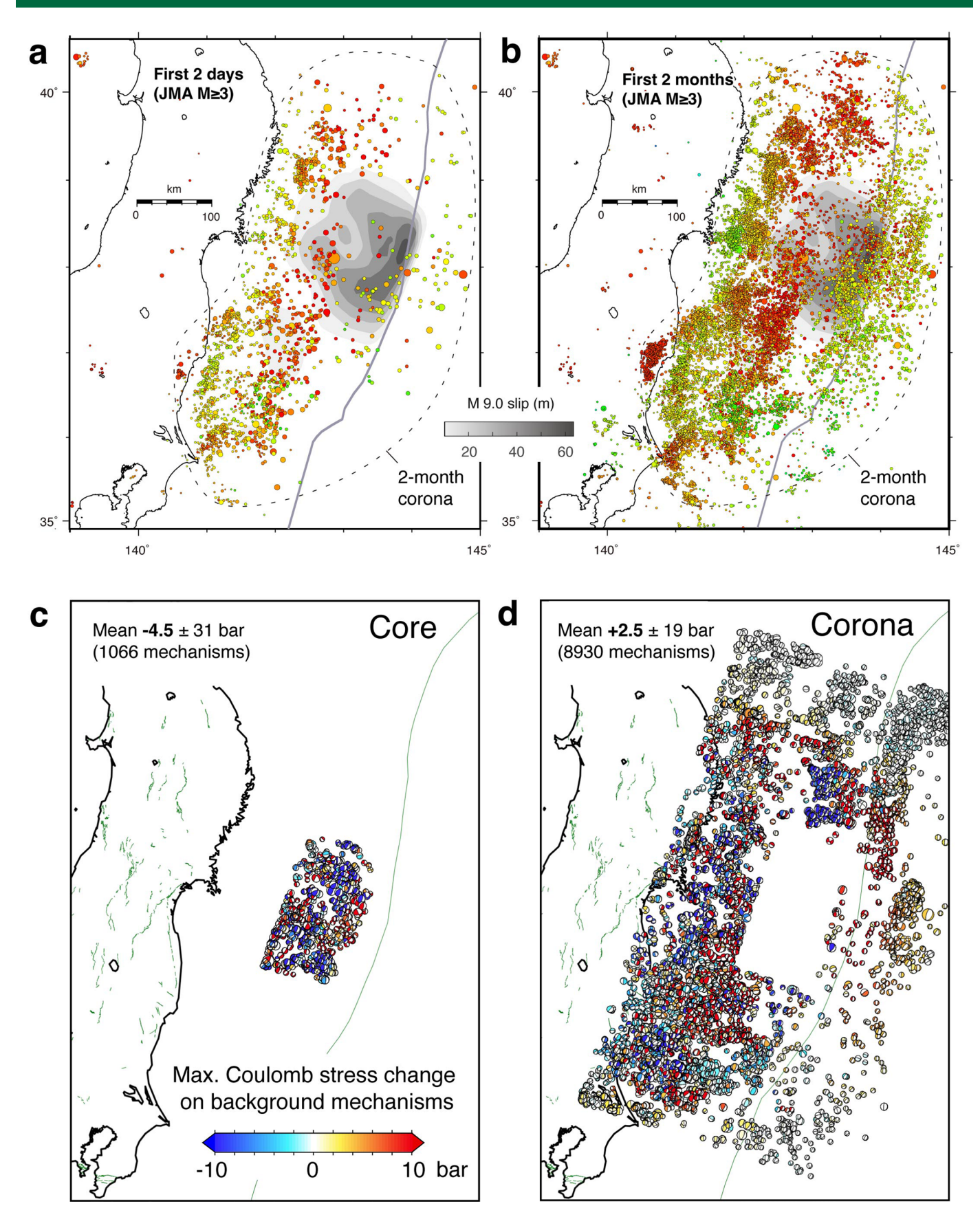


Extended Data Fig. 1 | Seismicity time series in the simplified corona and core areas. a, Map of the seismicity rate change. The 13 Feb M 7.1, 20 Mar M 7.1, and 1 May M 6.9 earthquakes in 2021 are shown as stars. b, Time series of earthquakes in the corona. Notice that the post-M 9 rate in the core has remained low for twice the duration of the several low-rate preseismic periods. c, Time series of earthquakes in the core. We use quartiles to evaluate uncertainty because the rates are not normally distributed. d-e, Omori decay parameters fitted using ref. ¹⁸. Notice the smaller earthquakes and steeper decay (p exponent) in the core than in the corona.

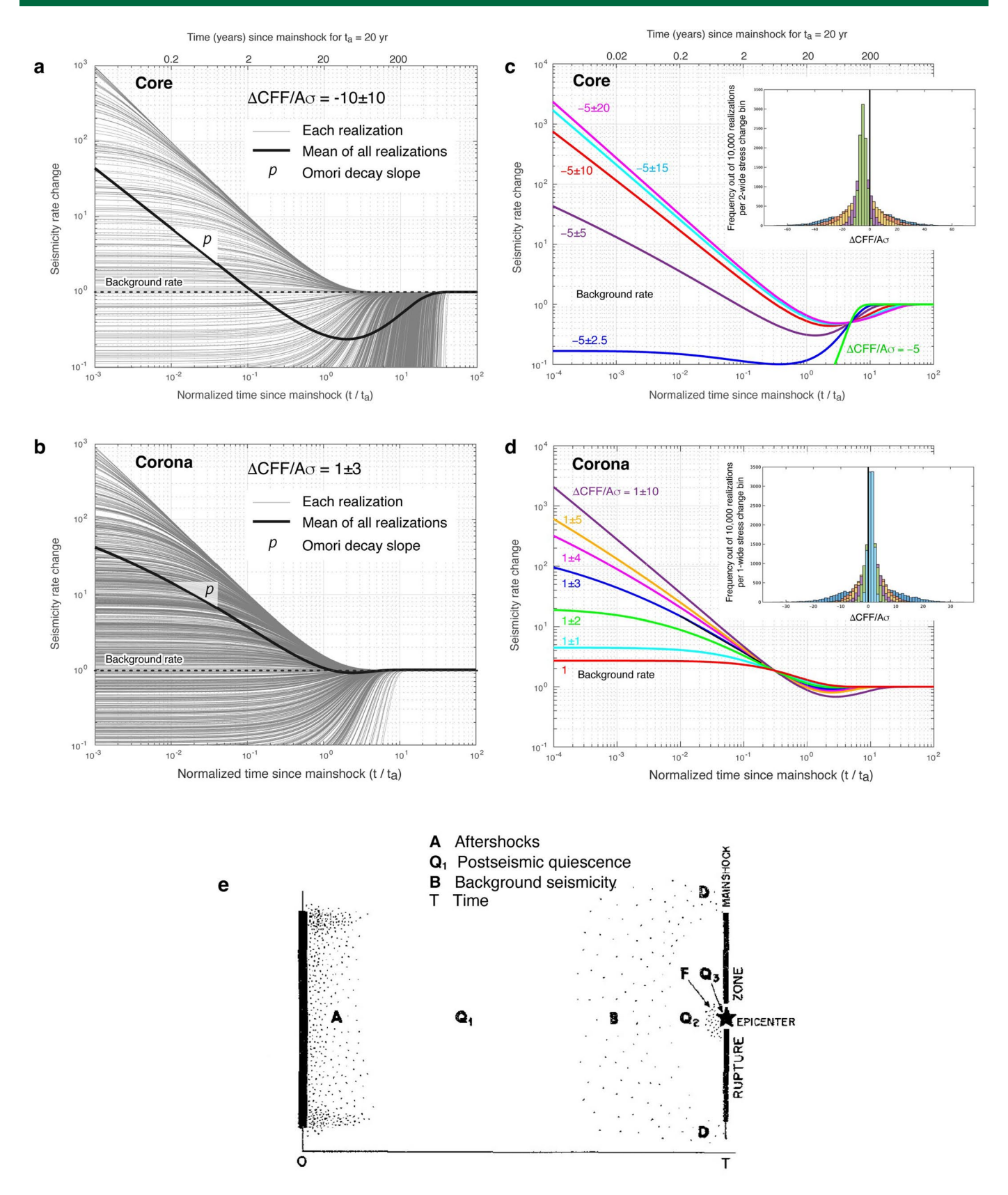


Extended Data Fig. 2 | See next page for caption.

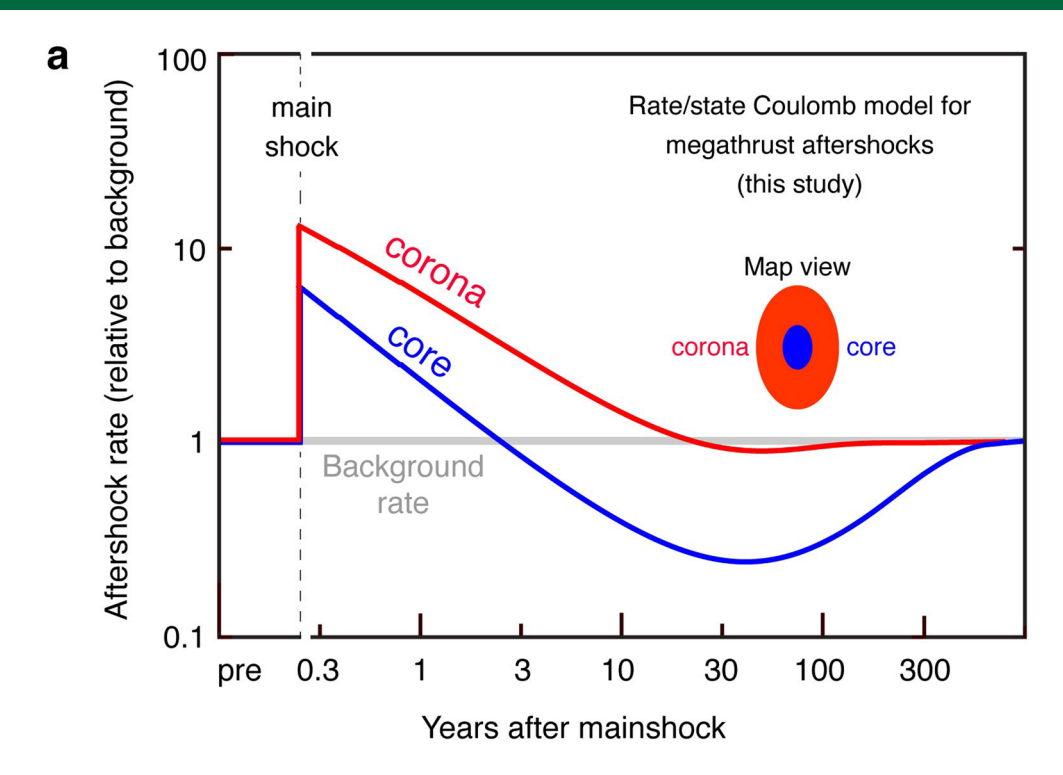
Extended Data Fig. 2 | Relationship between seismicity rate change and postseismic slip. a, Seismicity rate change for 2003 Tokachi-Oki, with coseismic 57 and postseismic slip during the first year 34 . Here we compare the period 5-10 yr after the quake (2008/09/26 - 2011/03) to the 5.7-yr background period (1998/01/01-2003/09/25). b. Seismicity associated with 2010 Maule (ANSS $M \ge 4.5$ catalog), with coseismic 59 and postseismic slip 61 . c, Postseismic slip during the first 8 months after 2011 Tohoku 32 superimposed on Figs. 1a and 2a. Panel **a** (right) adapted with permission from ref. 34 , Springer Nature Limited. Panel **b** (right) reproduced with permission from ref. 59 , John Wiley and Sons.

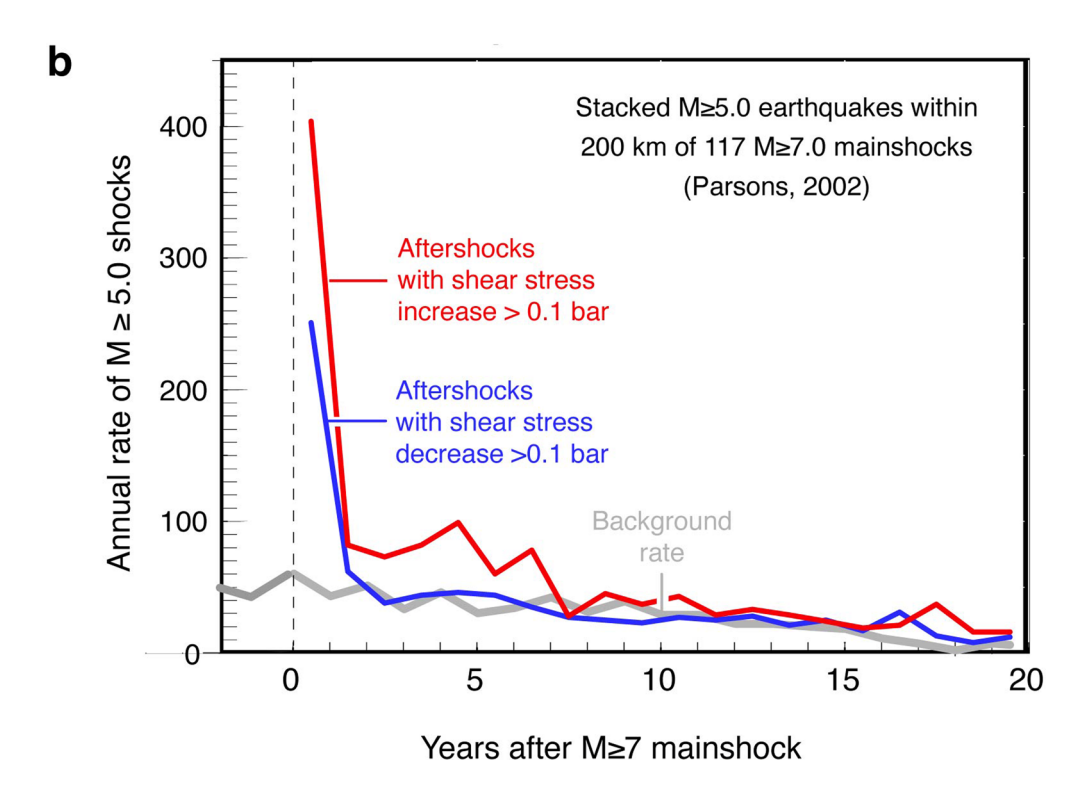


Extended Data Fig. 3 | Corona growth with time, and Coulomb stress imparted to focal mechanisms in the core and corona. a-b, Two-day and two-month corona extent. c, Simplified core area with beachballs colored by maximum Coulomb stress change. Because for each mechanism, we take the nodal plane with the most positive (maximum) stress change, these results could be biased toward stress increases. Mechanisms from 1998/01/01 - 2011/03/10, $M \ge 3$, depth ≤ 150 km, from F-Net catalog.

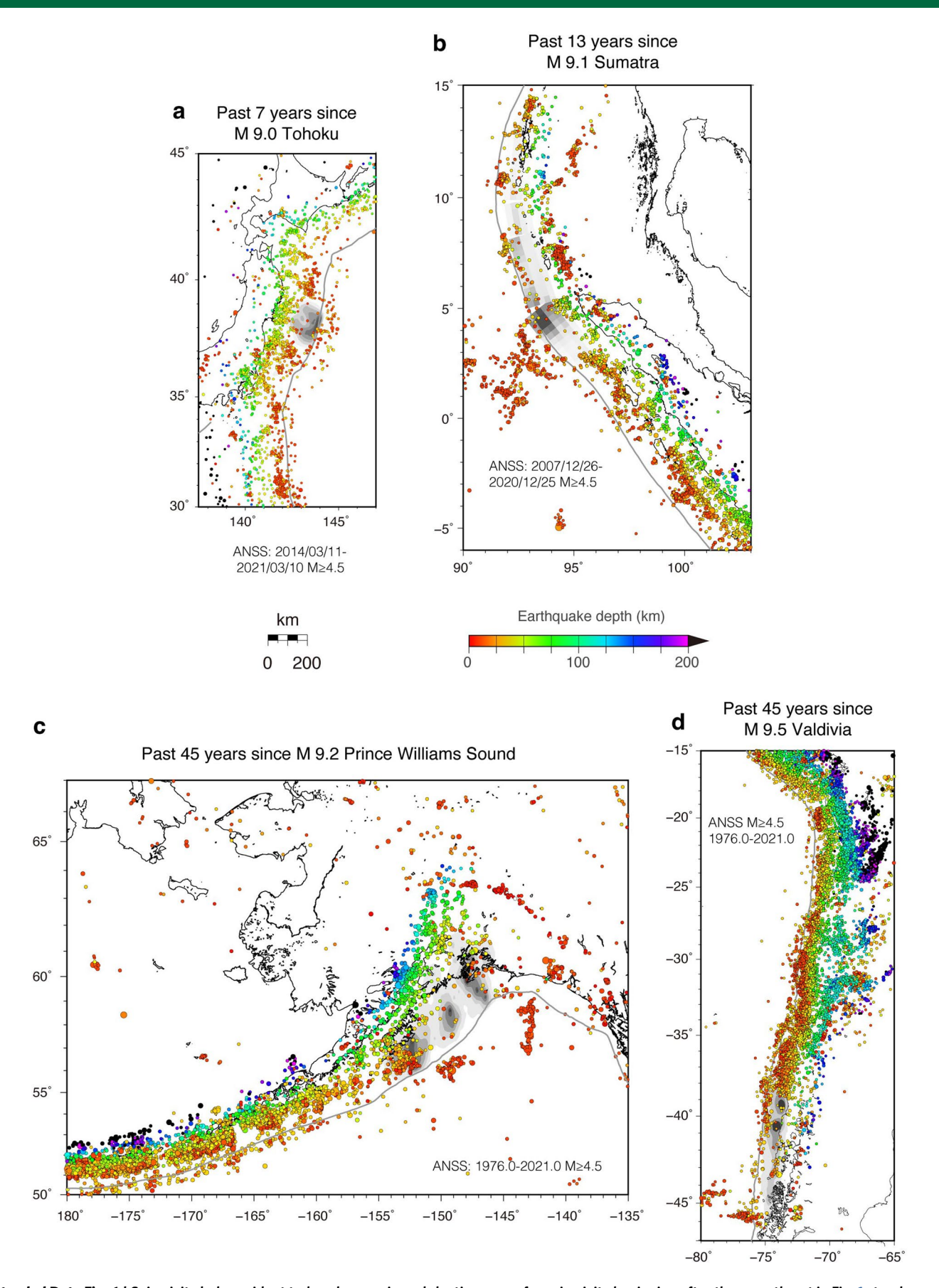


Extended Data Fig. 4 | Model of seismicity evolution in a heterogeneous faulting environment. a, Simulated time histories given a standard deviation 3 times larger than a mean stress decrease. t_a is the aftershock duration in rate/state friction. Each curve is a mean of 10,000 Monte Carlo simulations. b, Time history given a standard deviation equal to a mean stress increase. c-d, Time histories under different assumptions for the mean and standard deviation of the stress changes. e, Figure from Scholz (1988)²⁶. The concentration of longer-lasting aftershocks at the periphery resembles our corona, while the briefer aftershocks (A) that fade into quiescence (Q1) at a rate lower than the background (B) resemble our core. Panel e adapted with permission from ref. ²⁶, Springer Nature Limited.

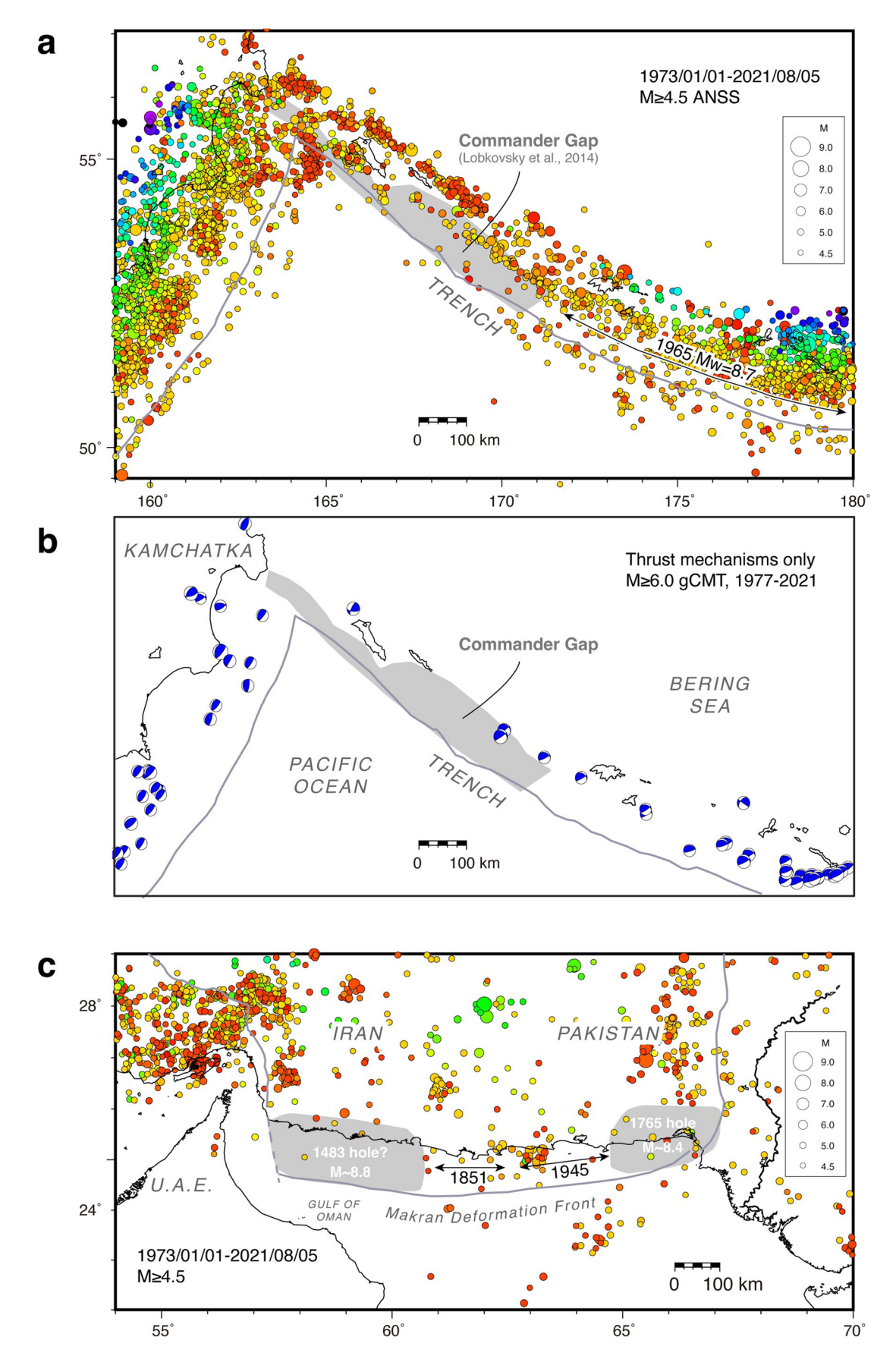




Extended Data Fig. 5 | Comparison of our model with results of Parsons (2002). a, This study. b, Fig. 9 of Parsons (2002). For simplicity, we have colored the curves and removed the uncertainty bounds. Parsons reported that aftershocks with shear stress increases (red curve, b) tend to locate 25 km father from the moment centroids than aftershocks with the shear stress decreases (blue curve, b). Thus, the decreases could occur in or near the core, and the increases in or near the corona.

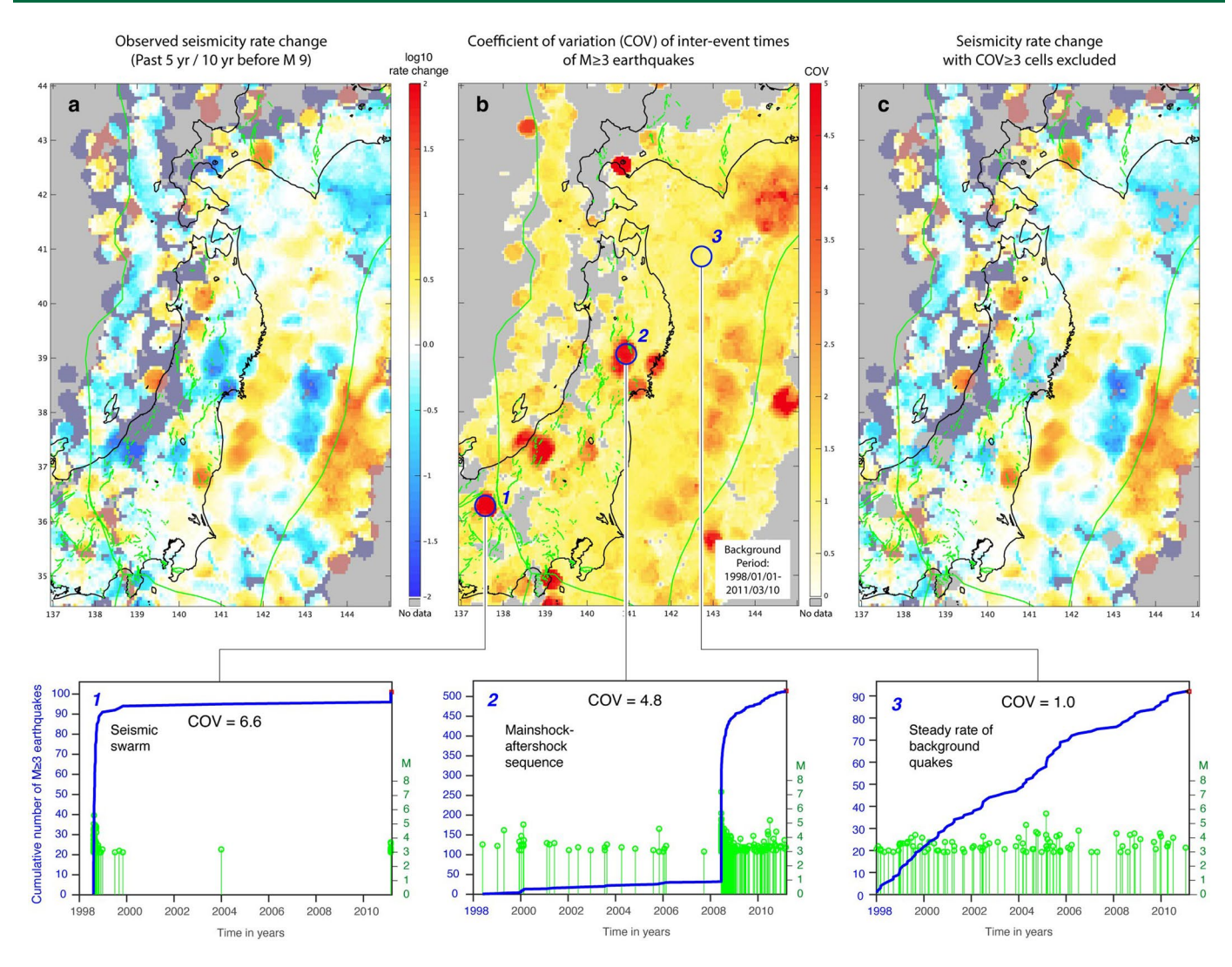


Extended Data Fig. 6 | Seismicity holes evident today along major subduction zones for seismicity beginning after the megathrust in Fig. 1 struck.a, Japan Trench, b, Sunda Trench, c, Alaska-Aleutian Trench, d, Peru-Chile Trench. For c-d, we begin when the seismic catalog detection markedly improves in about 1976. All maps are at the same scale.

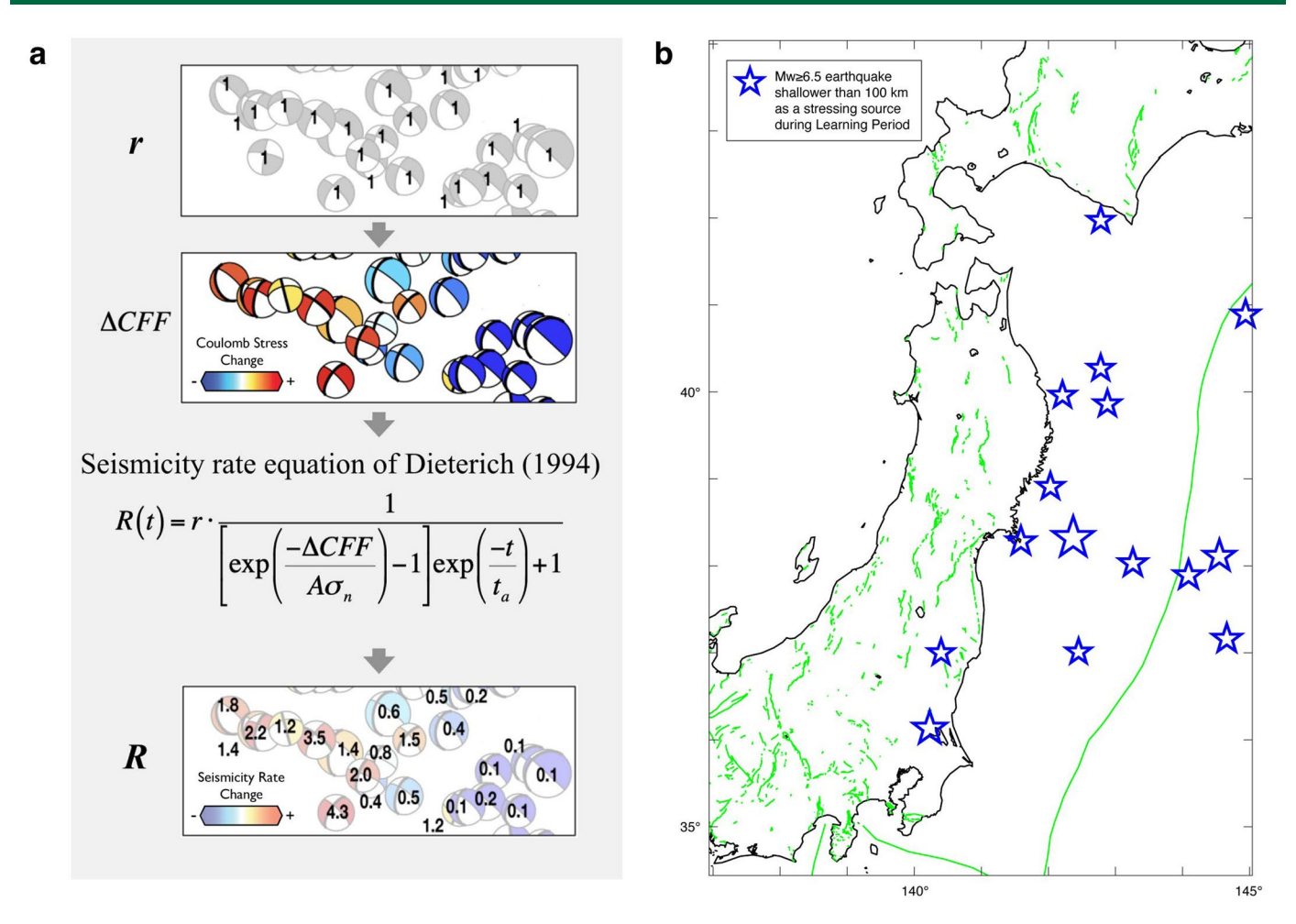


Extended Data Fig. 7 | See next page for caption.

Extended Data Fig. 7 | Seismicity holes associated with candidate historic or prehistoric megathrust earthquakes. a, The Commander (Komandor) Seismic Gap extends for 700 km along the northwest Aleutian Trench^{41, 60}, where oblique slip is partitioned between subduction convergence and a parallel back-arc transform fault. b, The hole is most evident for subduction mechanisms⁶. c, The Makran Deformation Front (Makran Trench) appears to have two holes, the eastern hole at the site of a 1765 earthquake, and the western hole perhaps associated with the debated 1483 earthquake^{42, 61, 62}.



Extended Data Fig. 8 | Masking swarms and secondary aftershocks in the seismicity rate change map. a, All data. b, Map of coefficient of variation of seismicity inter-event times with site 1 for a seismic swarm and site 2 aftershocks of a secondary mainshock during the pre-M 9 period, and site 3, steady background seismicity. c, Same as a but with sites of $COV \ge 3$ masked.



Extended Data Fig. 9 | Schematic illustration of how seismicity rate changes are derived from stress imparted to focal mechanisms. a, Each focal mechanism is a proxy for a small-to-moderate fault on which that earthquake stuck (top panel in a). These earthquakes then receive coseismic stress from a nearby mainshock (second panel in a), some promoting failure (red) and some inhibiting failure (blue). The applied stress amplifies or diminishes the background seismicity rate (bottom panel in a), according the the seismicity rate equation²¹. Finally, to make a map of forecast seismicity as in Fig. 2b, the updated numbers on the focal mechanism plots in the bottom panel in a are spatially smoothed by a moving kernel on the grid nodes. This illustration is from ref. ⁵⁶. b, Map of the Learning Period earthquakes ($M \ge 6.5$ during 3-11-2011 to 3-10-2016) that are used in the model. Panel **a** reproduced with permission from ref. ⁴⁵, Seismological Society of America.